Computational Condensed Matter 4 (2015) 46–58

Contents lists available at ScienceDirect

Computational Condensed Matter

journal homepage: http://ees.elsevier.com/cocom/default.asp

Regular article

Phase field crystal modeling of ternary solidification microstructures

Marco Berghoff [a, *], Britta Nestler [a, b]

[a] Institute of Applied Materials (IAM), Karlsruhe Institute of Technology (KIT), Karlsruhe, Germany
[b] Institute of Materials and Processes (IMP), Karlsruhe University of Applied Sciences, Karlsruhe, Germany

ARTICLE INFO

Article history:
Received 17 June 2015
Received in revised form
24 August 2015
Accepted 25 August 2015
Available online 6 September 2015

2010 MSC:
80A30
34Nxx
00A72
00A79

Keywords:
Multi-component phase-field crystal
Ternary eutectic lamellar growth
Energy minimization
Eutectic phase diagram
Atomic diffusion

ABSTRACT

In the present work, we present a free energy derivation of the multi-component phase-field crystal model [1] and illustrate the capability to simulate dendritic and eutectic solidification in ternary alloys. Fast free energy minimization by a simulated annealing algorithm of an approximated crystal is compared with the free energy of a fully simulated phase field crystal structure. The calculation of ternary phase diagrams from these free energies is described. Based on the free energies related to the ternary Al–Cu–Mg system, we show phase field crystal simulations of both, ternary dendritic growth as well as lamellar eutectic growth of three distinct solid phases.

1. Introduction

In the last years, simulations of atomistic effects have become an important field in materials research. For this purpose, density functional theory (DFT) and molecular dynamics (MD) are the classic methods. On a larger scale, the phase field method (PFM) can be used for simulations of microstructure formations up to several micrometers. Through continuous consideration, the effects on a smaller scale are no longer modeled, but their effects are taken into account. As shown in Ref. [2], details are lost, however, and the results between MD and PFM are comparable to each other. Elder et al. [3,4] introduce a continuous field of the probability density of atomic presence, by adapting the Swift–Hohenberg–Equation [5] and later approximating the functional of DFT. In line of these approaches, the phase field crystal (PFC) method is able to reproduce results of DFT and MD such as the physics of grain boundaries [6], elastic and plastic deformations [4] and thermodynamics of iron [7] and fcc metals [8]. In terms of time, PFC lies between DFT, MD and PFM, although PFC can be regarded as the time average of MD [9]. While the normal PFC acting on the atomic length scale, a PFC for colloids is proposed in Ref. [10] and operates on the length scale resolving colloidal structures. The extension to two components [11] allows the simulation of lamellar eutectic structures [12]. The multi-component PFC was introduced as a consequence, in the style of the multi-component PFM by Ofori–Opoku et al. [1].

In Sec. 2, we derive the multi-component PFC from DFT, point out the assumptions and elaborate the implementation scheme. In the following Sec. 3, we exhibit the calculation of ternary phase diagrams using the analytical expression of the free energies for a unit cell. Based on the model preparations, we apply the PFC simulation framework in Sec. 4 to compute 2D and 3D ternary dendrites and eutectic lamellae. We finally draw conclusion of the results.

2. Multi-component PFC model

The basis of the multi-component PFC model (MPFC) is the free energy functional for a pure material given by

* Corresponding author.
E-mail address: marco.berghoff@kit.edu (M. Berghoff).

http://dx.doi.org/10.1016/j.cocom.2015.08.002

$$\frac{\Delta\mathscr{F}}{k_BT} = \int \rho(\boldsymbol{r})\ln\left(\frac{\rho(\boldsymbol{r})}{\rho_\ell}\right) - \delta\rho(\boldsymbol{r})\mathrm{d}\boldsymbol{r} - \frac{1}{2}\int \delta\rho(\boldsymbol{r})C_2(|\boldsymbol{r},\boldsymbol{r}'|)\delta\rho(\boldsymbol{r}')\mathrm{d}\boldsymbol{r}\mathrm{d}\boldsymbol{r}' + \cdots,$$

where the dots stand for the omitted correlations of higher order. As is usual in the pure case, only excess energy contributions of pairwise correlations are taken into consideration, even for the multi-component free energy functional. For K types of atom, the free energy functional can be modeled as the sum of K pure, free energy functionals $\Delta\mathscr{F}_i$, $i \in \{1,\ldots,K\}$ and additional coupling terms between two types of atom a time according to

$$\frac{\Delta\mathscr{F}}{k_BT} = \sum_i \frac{\Delta\mathscr{F}_i}{k_BT} - \sum_{i<j}\int \delta\rho_i(\boldsymbol{r})C_2^{ij}(\boldsymbol{r},\boldsymbol{r}')\delta\rho_j(\boldsymbol{r}')\mathrm{d}\boldsymbol{r}'\mathrm{d}\boldsymbol{r}$$

with C_2^{ij} being the pairwise correlation functions between i–j atoms. We write the free energy as a sum of the ideal energy density ΔF_{id} comprising entropy contributions for an K-component system and the excess energy density ΔF_{ex}, which is based on the interactions of the atoms. This yields

$$\frac{\Delta\mathscr{F}}{k_BT} = \int \frac{\Delta F_{\mathrm{id}}}{k_BT} + \frac{\Delta F_{\mathrm{ex}}}{k_BT}\mathrm{d}\boldsymbol{r},$$

with

$$\frac{\Delta F_{\mathrm{id}}}{k_BT} = \sum_i \rho_i\ln\left(\frac{\rho_i}{\rho_{\ell i}}\right) - \delta\rho_i \tag{1}$$

and

$$\frac{\Delta F_{\mathrm{ex}}}{k_BT} = -\frac{1}{2}\int \sum_{i,j}\delta\rho_i(\boldsymbol{r})C_2^{ij}(\boldsymbol{r},\boldsymbol{r}')\delta\rho_j(\boldsymbol{r}')\mathrm{d}\boldsymbol{r}'. \tag{2}$$

Here, ρ_i represents the density for the component i and $\rho_{\ell i}$ is the reference density in the liquid phase during coexistence. $\delta\rho_i := \rho_i - \rho_{\ell i}$ is the difference in density. In order to get a similarity to the phase field model, we define the total mass density $\rho := \sum_i \rho_i$, the total reference mass density $\rho_\ell := \sum_i \rho_{\ell i}$, the concentrations $c_i := \frac{\rho_i}{\rho}$, the corresponding reference concentrations $c_{\ell i} := \frac{\rho_{\ell i}}{\rho_\ell}$ and the dimensionless mass density $n := \frac{\rho-\rho_\ell}{\rho_\ell}$. With these definitions, the condition $\sum_i c_i = 1$ is fulfilled and Eq. (1) results in

$$\frac{\Delta F_{\mathrm{id}}}{k_BT} = \rho_\ell\left((n+1)\ln(n+1) - n + (n+1)\sum_i c_i\ln\left(\frac{c_i}{c_{\ell i}}\right)\right).$$

We denote the ideal mixing entropy density by

$$\Delta F_{\mathrm{mix}}(\boldsymbol{c}) := \sum_i c_i\ln\left(\frac{c_i}{c_{\ell i}}\right)$$

and with the Taylor expansion for $\ln(n+1)$, we get

$$\frac{\Delta F_{\mathrm{id}}}{k_BT\rho_\ell} = \frac{n^2}{2} - \frac{n^3}{6} + \frac{n^4}{12} + (n+1)\Delta F_{\mathrm{mix}}. \tag{3}$$

Assuming that the correlation functions $C_2^{ij}(\boldsymbol{r},\boldsymbol{r}')$ are isotropic, the correlation functions only depend on the value of $|\boldsymbol{r}-\boldsymbol{r}'|$ and hence $C_2^{ij} = C_2^{ji}$. We write $C_2^{ij}(\boldsymbol{r}-\boldsymbol{r}')$.

We next consider a single term of the sum in Eq. (2) for an arbitrary $i,j \in [1,K]$ using the definitions and introducing the short notation $\cdot'$ for the dependence on $\boldsymbol{r}'$ we obtain

$$-\frac{1}{2}\int \delta\rho_i C_2^{ij}\delta\rho_j'\mathrm{d}\boldsymbol{r}' = -\frac{1}{2}(\rho_i - \rho_{\ell i})\rho_l\int C_2^{ij}c_j'n\prime + C_2^{ij}c_j' - C_2^{ij}c_{\ell j}'\mathrm{d}\boldsymbol{r}'. \tag{4}$$

The density n is periodic with the lattice constant, whereas c_j is an extensive field. As proposed in Refs. [12,13], we consider a first approximation of these contributions of the form

$$\int C_2^{ij}(\boldsymbol{r}-\boldsymbol{r}')n(\boldsymbol{r}')c_j(\boldsymbol{r}')\mathrm{d}\boldsymbol{r}' \approx c_j(\boldsymbol{r})\int C_2^{ij}(\boldsymbol{r}-\boldsymbol{r}')n(\boldsymbol{r}')\mathrm{d}\boldsymbol{r}'.$$

We integrate by substitution for multiple variables and using the substitution $\boldsymbol{t} := \boldsymbol{r} - \boldsymbol{r}'$. The associated functional determinant $\det(D\boldsymbol{t}) = (-1)^K$, and hence, the following equation applies:

$$\int C_2^{ij}(\boldsymbol{r}-\boldsymbol{r}')c_{\ell j}\mathrm{d}\boldsymbol{r}' = c_{\ell j}\int C_2^{ij}(\boldsymbol{t})\mathrm{d}\boldsymbol{t}.$$

Because the substitution is linear, we do not consider the integration boundaries any further. Applying the Fourier transform results in

$$c_{\ell j}\int C_2^{ij}(\boldsymbol{t})\cdot 1\mathrm{d}\boldsymbol{t} = c_{\ell j}\int C_2^{ij}(\boldsymbol{t})\cdot \mathrm{e}^{-i\boldsymbol{k}\cdot\boldsymbol{t}}\mathrm{d}\boldsymbol{t}|_{\boldsymbol{k}=0} = c_{\ell j}\widehat{C}_2^{ij}(0)$$

with $\widehat{C}_2^{ij}(\boldsymbol{k})$ as the Fourier transform of C_2^{ij}.

We redefine $C_2^{ij} := \rho_\ell C_2^{ij}$. The prefactor in Eq. (4), can be written as $\rho_i - \rho_{\ell i} = c_i\rho_\ell(n+1) - c_{\ell i}\rho_l = \rho_\ell(c_i(n+1) - c_{\ell i})$. Integration over $\boldsymbol{r}$ results in the excess energy

$$\begin{aligned}\frac{\Delta\mathscr{F}_{\mathrm{ex}}}{k_BT\rho_\ell} = &-\frac{1}{2}\sum_{i,j}\int (c_in + c_i - c_{\ell i})c_j\int C_2^{ij}n'\mathrm{d}\boldsymbol{r}'\mathrm{d}\boldsymbol{r}\\ &-\frac{1}{2}\sum_{i,j}\int (c_in + c_i - c_{\ell i})\int C_2^{ij}c_j'\mathrm{d}\boldsymbol{r}'\mathrm{d}\boldsymbol{r}\\ &+\frac{1}{2}\sum_{i,j}\int (c_in + c_i - c_{\ell i})c_{\ell j}\widehat{C}_2^{ij}(0)\mathrm{d}\boldsymbol{r}.\end{aligned} \tag{5}$$

According to Refs. [11,14–16] all terms of linear order in n and n' disappear in Eq. (5). We calculate the term with the coupling of c_i and c_j with C_2^{ij} of Eq. (5) for any i, j by

$$\mathscr{A}_{ij} := \int c_i(\boldsymbol{r})\int C_2^{ij}(\boldsymbol{r}-\boldsymbol{r}')c_j(\boldsymbol{r}')\mathrm{d}\boldsymbol{r}'\mathrm{d}\boldsymbol{r}. \tag{6}$$

We can write the correlation function as an inverse Fourier transform of $\widehat{C}_2^{ij}$

$$C_2^{ij}(\boldsymbol{r}-\boldsymbol{r}') = \int \widehat{C}_2^{ij}(\boldsymbol{k})\mathrm{e}^{i\boldsymbol{k}\cdot(\boldsymbol{r}-\boldsymbol{r}')}\mathrm{d}\boldsymbol{k} = \int \widehat{C}_2^{ij}(\boldsymbol{k})\mathrm{e}^{i\boldsymbol{k}\cdot\boldsymbol{r}}\mathrm{e}^{-i\boldsymbol{k}\cdot\boldsymbol{r}'}\mathrm{d}\boldsymbol{k}. \tag{7}$$

Inserting Eq. (7) in Eq. (6) yields

$$\begin{aligned}\mathscr{A}_{ij} &= \int c_i(\boldsymbol{r})\iint \widehat{C}_2^{ij}(\boldsymbol{k})\mathrm{e}^{i\boldsymbol{k}\cdot\boldsymbol{r}}\mathrm{e}^{-i\boldsymbol{k}\cdot\boldsymbol{r}'}\mathrm{d}\boldsymbol{k}c_j(\boldsymbol{r}')\mathrm{d}\boldsymbol{r}'\mathrm{d}\boldsymbol{r}\\ &= \int c_i(\boldsymbol{r})\int \widehat{C}_2^{ij}(\boldsymbol{k})\mathrm{e}^{i\boldsymbol{k}\cdot\boldsymbol{r}}\int c_j(\boldsymbol{r}')\mathrm{e}^{-i\boldsymbol{k}\cdot\boldsymbol{r}'}\mathrm{d}\boldsymbol{r}'\mathrm{d}\boldsymbol{k}\mathrm{d}\boldsymbol{r}\\ &= \int c_i(\boldsymbol{r})\int \widehat{C}_2^{ij}(\boldsymbol{k})\widehat{c}_j(\boldsymbol{k})\mathrm{e}^{i\boldsymbol{k}\cdot\boldsymbol{r}}\mathrm{d}\boldsymbol{k}\mathrm{d}\boldsymbol{r},\end{aligned}$$

where $\widehat{c}_j$ is the Fourier transform of c_j. For the long-wave limit consideration, we expand the correlation function in exponential numbers of $\boldsymbol{k}^2$ at $\boldsymbol{k} = 0$ by

$$\mathscr{A}_{ij} = \int c_i(\boldsymbol{r}) \int \sum_l \frac{1}{l!} \boldsymbol{k}^{2l} \frac{\partial^l \widehat{C}_2^{ij}(\boldsymbol{k})}{\partial (\boldsymbol{k}^2)^l}\bigg|_{\boldsymbol{k}=0} \widehat{c}_j(\boldsymbol{k}) \mathrm{e}^{i\boldsymbol{k}\cdot\boldsymbol{r}} \mathrm{d}\boldsymbol{k}\mathrm{d}\boldsymbol{r}.$$

We further consider the leading terms up to order $l = 1$ and approximate the summation expansion by

$$\begin{aligned}\mathscr{A}_{ij} \approx & \int c_i(\boldsymbol{r}) \int \widehat{C}_2^{ij}(\boldsymbol{k})|_{\boldsymbol{k}=0} \widehat{c}_j(\boldsymbol{k}) \mathrm{e}^{i\boldsymbol{k}\cdot\boldsymbol{r}} \mathrm{d}\boldsymbol{k}\mathrm{d}\boldsymbol{r} \\ & + \int c_i(\boldsymbol{r}) \int \boldsymbol{k}^2 \frac{\partial \widehat{C}_2^{ij}(\boldsymbol{k})}{\partial (\boldsymbol{k}^2)}\bigg|_{\boldsymbol{k}=0} \widehat{c}_j(\boldsymbol{k}) \mathrm{e}^{i\boldsymbol{k}\cdot\boldsymbol{r}} \mathrm{d}\boldsymbol{k}\mathrm{d}\boldsymbol{r}.\end{aligned} \tag{8}$$

By introducing the notations

$$\gamma_{ij} := \widehat{C}_2^{ij}(\boldsymbol{k})|_{\boldsymbol{k}=0},$$

$$\kappa_{ij} := \frac{\partial \widehat{C}_2^{ij}(\boldsymbol{k})}{\partial (\boldsymbol{k}^2)}\bigg|_{\boldsymbol{k}=0}$$

and by applying the inverse Fourier transforms in Eq. (8) leads to

$$\mathscr{A}_{ij} = \gamma_{ij} \int c_i(\boldsymbol{r}) c_j(\boldsymbol{r}) \mathrm{d}\boldsymbol{r} + \kappa_{ij} \int c_i(\boldsymbol{r}) \left(-\nabla^2\right) c_j(\boldsymbol{r}) \mathrm{d}\boldsymbol{r}$$

With Gauss's theorem the second integral becomes

$$-\int_\Omega c_i(\boldsymbol{r}) \nabla\cdot\nabla c_j(\boldsymbol{r}) \mathrm{d}\boldsymbol{r} = -\int_{\delta\Omega} c_i(\boldsymbol{r}) \nabla c_j(\boldsymbol{r}) \cdot \boldsymbol{n} \mathrm{d}S + \int_\Omega \nabla c_i(\boldsymbol{r}) \cdot \nabla c_j(\boldsymbol{r}) \mathrm{d}\boldsymbol{r}$$

with $\boldsymbol{n}$ the outward pointing unit normal field of the boundary $\delta\Omega$. The integral over the boundary vanishes for periodic domains, or Ω is chosen large enough. It follows

$$\mathscr{A}_{ij} = \gamma_{ij} \int c_i(\boldsymbol{r}) c_j(\boldsymbol{r}) \mathrm{d}\boldsymbol{r} + \kappa_{ij} \int \nabla c_i(\boldsymbol{r}) \cdot \nabla c_j(\boldsymbol{r}) \mathrm{d}\boldsymbol{r}. \tag{9}$$

Similarly to the calculus in Eqs. (6)–(9), the expression with the coupling of $c_{\mathfrak{l}i}$ and c_j with C_2^{ij} of Eq. (5) can be simplified, for any desired i, j by

$$\begin{aligned}\mathscr{B}_{ij} := & \int c_{\mathfrak{l}i}(\boldsymbol{r}) \int C_2^{ij}(\boldsymbol{r}-\boldsymbol{r}') c_j(\boldsymbol{r}') \mathrm{d}\boldsymbol{r}' \mathrm{d}\boldsymbol{r} \\ \approx & \gamma_{ij} \int c_{\mathfrak{l}i}(\boldsymbol{r}) c_j(\boldsymbol{r}) \mathrm{d}\boldsymbol{r} + \kappa_{ij} \int \nabla c_{\mathfrak{l}i}(\boldsymbol{r}) \cdot \nabla c_j(\boldsymbol{r}) \mathrm{d}\boldsymbol{r}.\end{aligned}$$

Taking into account that $c_{\mathfrak{l}i}$ is constant, it follows that

$$\mathscr{B}_{ij} = \gamma_{ij} \int c_{\mathfrak{l}i} c_j(\boldsymbol{r}) \mathrm{d}\boldsymbol{r}. \tag{10}$$

Considering the definition of γ_{ij}, it can be seen that $\mathscr{B}_{ij}$ is of the same form as the last term in Eq. (5). We insert the simplifications of $\mathscr{A}_{ij}$ (Eq. (9)) and $\mathscr{B}_{ij}$ (Eq. (10)) in Eq. (5) and derive

$$\begin{aligned}\frac{\Delta F_{\mathrm{ex}}}{k_B T \rho_{\mathfrak{l}}} = & -\frac{1}{2}\sum_{i,j} \int n c_i c_j \int C_2^{ij} n' \mathrm{d}\boldsymbol{r}' \mathrm{d}\boldsymbol{r} - \frac{1}{2}\sum_{i,j} \kappa_{ij} \int \nabla c_i \cdot \nabla c_j \mathrm{d}\boldsymbol{r} \\ & - \frac{1}{2}\sum_{i,j} \int \left(-(c_i n + c_i - c_{\mathfrak{l}i}) c_{\mathfrak{l}j} - c_{\mathfrak{l}i} c_j + c_i c_j\right) \gamma_{ij} \mathrm{d}\boldsymbol{r} \\ = & \int -\frac{1}{2} n \int \sum_{i,j} c_i c_j C_2^{ij} n' \mathrm{d}\boldsymbol{r}' - \frac{1}{2}\sum_{i,j} \kappa_{ij} \nabla c_i \cdot \nabla c_j - \frac{1}{2}\sum_{i,j} \Gamma_{ij} \gamma_{ij} \mathrm{d}\boldsymbol{r},\end{aligned} \tag{11}$$

with $\Gamma_{ij} := -(c_i n + c_i - c_{\mathfrak{l}i}) c_{\mathfrak{l}j} - c_{\mathfrak{l}i} c_j + c_i c_j$.

With this formulation, we summarize the ideal energy in Eq. (3) and the excess energy in Eq. (11) by

$$\begin{aligned}\mathscr{F} = & \int \frac{n^2}{2} - \eta \frac{n^3}{6} + \chi \frac{n^4}{12} + \omega(n+1)\Delta F_{\mathrm{mix}} \\ & - \frac{1}{2} n \int \sum_{i,j} c_i c_j C_2^{ij} n' \mathrm{d}\boldsymbol{r}' - \frac{1}{2}\sum_{i,j} \kappa_{ij} \nabla c_i \cdot \nabla c_j \mathrm{d}\boldsymbol{r},\end{aligned} \tag{12}$$

where the constants η, χ and ω are introduced. These constants are formally equal to one, but may, however, allow additional degrees of freedom that can be used to correct the density dependence of the ideal free energy away from the reference density ρ_0, to match materials properties, as shown by Ref. [11]. To keep the form of the free energy compact, Ofori–Opoku et al. [1] have found that it is simpler to introduce a parameter ω, which modifies the mixing free energy from its ideal form, away from the reference compositions c_i^0. So we can combine the last term in Eq. (11) with ΔF_{mix}. We introduce the abbreviation $\mathscr{F} := \frac{\Delta \mathscr{F}}{k_B T \rho_{\mathfrak{l}}}$.

2.1. Effective correlation function

The pairwise correlation functions C_2^{ij} in Eq. (12) only occur in the term

$$\int \sum_{i,j} c_i c_j C_2^{ij} n' \mathrm{d}\boldsymbol{r}'$$

and are weighted by $c_i c_j$. Higher-order correlations are neglected throughout the derivations, so that e.g. contributions $c_i c_j c_k C_3^{ijk}$ are not respected. The correlation functions of pure materials (C_2^{ii}) are much simpler than the cross correlations (C_2^{ij}, $i \neq j$), so we define an effective correlation function C_{eff}, which is interpolated with the concentrations c_i from the correlation functions for pure materials. In addition, we define $h_i(\boldsymbol{c})$ to be interpolation functions, so that C_{eff} has steady derivatives. Thus, we write

$$C_{\mathrm{eff}}(\boldsymbol{r}-\boldsymbol{r}') := \sum_i h_i(\boldsymbol{c}) C_2^{ii}(\boldsymbol{r}-\boldsymbol{r}').$$

The correlation function is defined directly in the Fourier space. For each family of symmetrically equivalent crystal planes, a peak, as defined by Greenwood et al. [17], arises of the form

$$\widehat{C}_{2,j}^{ii}(\boldsymbol{k}) := \mathrm{e}^{-\frac{\sigma^2}{\sigma_{M_{ij}}^2}} \mathrm{e}^{-\frac{\left(|\boldsymbol{k}| - \kappa_{ij}\right)^2}{2\alpha_{ij}^2}}. \tag{13}$$

The first two planes in a 2D square lattice are the families {10} and {11}, where $\lambda_1 = a$ is the distance of the {10}-planes and $\lambda_2 = a/\sqrt{2}$ is the distance of the {11}-planes. For an fcc lattice, the first planes are {111} and {200} with the distances $\lambda_1 = a/\sqrt{3}$ and $\lambda_2 = a/2$.

The first exponential function is a Debye–Waller factor, which

sets the effective temperature noted by σ. $\sigma_{M_{ij}}$ is an effective transition temperature, which describes the effects of the crystal plane. Greenwood et al. [18] use $\sigma^2_{M_{ij}} = \frac{2\rho_j\beta_j}{k^2_{ij}}$ with the atomic density ρ_j, the number of symmetrical planes β_j and the reciprocal lattice spacing $k_{ij} = 2\pi/\lambda_{ij}$ of the jth plane and the ith component.

The second exponential function is a Gaussian bell curve with a variance α^2_{ij} and a smoothed δ peak at the position k_{ij}. The denominator α_{ij} sets the elastic energy and the surface energy, as well as the anisotropic properties, as shown in Greenwood et al. [17]. For each family of crystal planes of a material i, a peak is added to the correlation function, which, represents the envelope of all peaks, given by

$$\widehat{C}^{ii}_2(\boldsymbol{k}) := \max_j \widehat{C}^{ii}_{2,j}(\boldsymbol{k}). \tag{14}$$

Fig. 1 shows the plot of the rotational invariant correlation functions $\widehat{C}^{ii}_2(k = |\boldsymbol{k}|)$ in Fourier space used for the solidification simulations in Sec. 4. In addition, the interpolated correlation function $\widehat{C}_{\text{eff}}$ for $\boldsymbol{c} = (0.3, 0.6, 0.1)$ is calculated and compared with three different interpolation functions. As calculated in Appendix A, the expression $h_i(\boldsymbol{c}) = 3c_i^2 - 2c_i^3 + 2c_i \sum_{j<k, j\neq i, k\neq i} c_j c_k$ (H1) used by Ofori–Opoku et al. [1] depends on the selection of the conditional variable. Therefore, we employ

$$h_i(\boldsymbol{c}) = \frac{c_i^2}{\sum_{j=1}^{K} c_j^2} \tag{H2}$$

by Moelans et al. [19] to conduct the simulations. A further interpolation function, published by Floch and Plapp [20], reads

$$h_i(\boldsymbol{c}) = \frac{c_i^2}{4}\Big(15(1-c_i)\Big(1 + c_i\big(c_j - c_k\big)^2\Big) + c_i\Big(9c_i^2 - 5\Big)\Big) \tag{H3}$$

with c_j and c_k as the other two concentrations. This fifth order polynomial is the lowest order polynomial which satisfies all the requirements in Appendix A. It is unique at this order. A drawback is that it only works for three concentrations. As seen in Fig. 1, the effective correlation function C_{eff} slightly depends on the used interpolation. The influence of the various interpolation functions is discussed in Sec. 4.1.

2.2. Dynamics of the multi-component PFC model

2.2.1. Onsager reciprocal relations

Onsager [21] postulated that the resulting force and the crossing forces act on the flow. By means of superposition, the resulting flow of the ith component becomes

$$j_i = -\sum_j L_{ij} \nabla \mu_j,$$

with L_{ii} for direct mass transport coefficients and L_{ij} for $i \neq j$ cross coefficients. We use the well known relation, as in Ref. [22],

$$L_{ij} := M_i c_i \left(\delta_{ij} - \frac{M_j c_j}{\sum_k M_k c_k}\right)$$

with diffusion coefficients M_i. Applying symmetry conditions, we obtain $L_{ij} = L_{ji}$ and $\sum_i L_{ij} = \sum_j L_{ij} = 0$.

According to Onsager, the symmetry properties retrieve the condition $\sum_i c_i = 1$ in the evolution equation of the concentrations

$$\frac{\partial c_i}{\partial t} = \nabla \cdot \sum_j L_{ij} \nabla \mu_j.$$

Since the chemical potentials μ_j are the variational derivatives of the free energy functional $\mathscr{F}$ according to c_j, the evolution equations for multiple concentrations result in

$$\begin{aligned}\frac{\partial c_i}{\partial t} &= \nabla \cdot \sum_j L_{ij} \nabla \frac{\delta \mathscr{F}}{\delta c_j} \\ &= \nabla \cdot \left(\sum_j L_{ij} \nabla \left(\omega(n+1)\frac{\delta \Delta F_{\text{mix}}}{\delta c_j} - \frac{1}{2} n \frac{\delta C_{\text{eff}}}{\delta c_j} * n + \kappa_j \nabla^2 c_j\right)\right),\end{aligned} \tag{15}$$

neglecting the terms for the cross gradients. We write $\kappa_j := \kappa_{jj}$ and use the abbreviated form of the convolutions

$$C_{\text{eff}} * n = \big(C_{\text{eff}} * n\big)(\boldsymbol{r}) = \int C_{\text{eff}}(\boldsymbol{r} - \boldsymbol{r}') n(\boldsymbol{r}') \mathrm{d}\boldsymbol{r}',$$

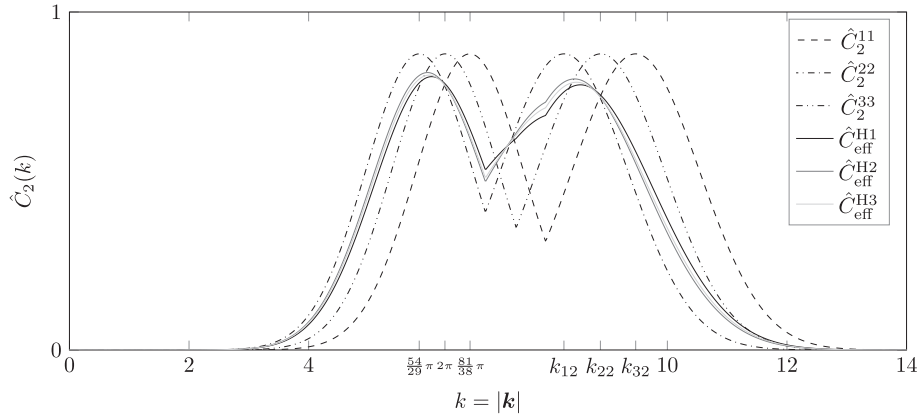

Fig. 1. The dashed curves correspond to pairwise correlation functions with the peaks at wave numbers $k_{11} = 81\pi/38$, $k_{21} = 54\pi/29$, $k_{31} = 2\pi$ and $k_{i2} = \sqrt{2}k_{i1}$, $i = 1,2,3$ for chosen values $\sigma_{M_{ij}} = 0.55$, $\alpha_{i1} = 0.8$ and $\alpha_{i2} = \sqrt{2}\alpha_{i1}$ $i = 1,2,3$. The grey and black solid curves display the effective correlation functions $\widehat{C}_{\text{eff}}$ for $\boldsymbol{c} = (0.1, 0.6, 0.3)$, interpolated with (H1), (H2) and (H3), respectively.

$$n\frac{\delta C_{\text{eff}}}{\delta c_j} * n = n(\boldsymbol{r})\left(\frac{\delta C_{\text{eff}}}{\delta c_j} * n\right)(\boldsymbol{r}) = n(\boldsymbol{r})\int \frac{\delta C_{\text{eff}}}{\delta c_j}(\boldsymbol{r}-\boldsymbol{r}')n(\boldsymbol{r}')\mathrm{d}\boldsymbol{r}'.$$

Conservation of density yields

$$\begin{aligned}\frac{\partial n}{\partial t}\frac{\partial n}{\partial t} &= \nabla\cdot\left(M_n\nabla\frac{\delta\mathscr{F}}{\delta n}\right)\\ &= \nabla\cdot\left(M_n\nabla\left(n-\eta\frac{n^2}{2}+\chi\frac{n^3}{3}+\omega\Delta F_{\text{mix}}-C_{\text{eff}}*n\right)\right).\end{aligned}\tag{16}$$

Since density and concentrations act on different length scales, the crossing forces between density and concentrations are neglected.

2.2.2. Operator splitting

We split the evolution equations Eqs. (15) and (16) into a linear and nonlinear part, as done in Ref. [23] for the binary case. For the density evolution, we write

$$\frac{\partial n}{\partial t} = (A_1 + A_2)n$$

with the suboperators

$$A_1 n = \nabla\cdot\left(M_n\nabla\left(-\eta\frac{n^2}{2}+\chi\frac{n^3}{3}+\omega\Delta F_{\text{mix}}-C_{\text{eff}}*n\right)\right),$$

$$A_2 n = \nabla\cdot M_n\nabla n.$$

For the concentrations, we first split the chemical potentials into a linear and nonlinear part by

$$\begin{aligned}\mu_j = \frac{\delta\mathscr{F}}{\delta c_j} &= \underbrace{\omega(n+1)\frac{\delta\Delta F_{\text{mix}}}{\delta c_j}-\frac{1}{2}n\frac{\delta C_{\text{eff}}}{\delta c_j}*n}_{=:\boldsymbol{c}_{\text{nl},j}} + \kappa_j\nabla^2 c_j\\ &= \boldsymbol{c}_{\text{nl},j} + \kappa_j\nabla^2 c_j.\end{aligned}$$

The evolution equations for the concentrations become

$$\begin{aligned}\frac{\partial c_i}{\partial t}\frac{\partial c_i}{\partial t} &= \nabla\cdot\sum_j L_{ij}\nabla\mu_j\\ &= \underbrace{\nabla\cdot\sum_j L_{ij}\nabla\boldsymbol{c}_{\text{nl},j} + (L_{ij}\kappa_j - S_{ij})\nabla^3 c_j}_{=:B_{i1}\boldsymbol{c}} + \underbrace{\sum_j S_{ij}\nabla^4 c_j}_{=:B_{i2}\boldsymbol{c}}\\ &= (B_{i1}+B_{i2})\boldsymbol{c},\end{aligned}$$

where S_{ij} are constants.

Time discretization takes place in Fourier space according to the equations

$$\frac{\partial\widehat{n}}{\partial t} = \left(\widehat{A}_1+\widehat{A}_2\right)\widehat{n},$$

$$\frac{\partial\widehat{c}_i}{\partial t} = \left(\widehat{B}_{i1}+\widehat{B}_{i2}\right)\widehat{\boldsymbol{c}}.$$

The quantities $\widehat{A}_1$, $\widehat{A}_2$, $\widehat{B}_{i1}$ and $\widehat{B}_{i2}$ are the corresponding operators,

$$\widehat{A}_2\widehat{n} = -M_n k^2\widehat{n},$$

$$\widehat{B}_{i2}\widehat{c}_i = \sum_j S_{ij}k^4\widehat{c}_j.$$

In a preliminary iteration step, the nonlinear parts are calculated in explicit intermediate states $(\widehat{n}^*, \widehat{c}_i^*)$ and subsequently, the new time step is calculated implicitly according to the following scheme

$$\widehat{n}^* = \widehat{n}^t + \Delta t\widehat{A}_1\widehat{n}^t,$$

$$\widehat{n}^{t+\Delta t} = \widehat{n}^* + \Delta t\widehat{A}_2\widehat{n}^{t+\Delta t},$$

$$\widehat{c}_i^* = \widehat{c}_i^t + \Delta t\widehat{B}_{i1}\widehat{\boldsymbol{c}}^t,$$

$$\widehat{c}_i^{t+\Delta t} = \widehat{c}_i^* + \Delta t\widehat{B}_{i2}\widehat{\boldsymbol{c}}^{t+\Delta t} = \widehat{c}_i^* + \sum_j \Delta t S_{ij}\widehat{\boldsymbol{c}}^{t+\Delta t}.$$

The implicit part for the density field can be resolved into the expression

$$\widehat{n}^{t+\Delta t} = \widehat{n}^*\Big/\left(1-\Delta t\widehat{A}_2\right).$$

For the concentration fields, we obtain the linear system of equations

$$A\widehat{\boldsymbol{c}}^{t+\Delta t} = \widehat{\boldsymbol{c}}^*,$$

with the matrix

$$A = \left(\delta_{ij} - \Delta t S_{ij}k^4\right)_{ij}.$$

The constants S_{ij} are chosen in such a way, that the contribution of the ∇^3 term is kept small and so the explicit step is as stable as possible. We define

$$S_{ij} := \left|\{L_{ij}(x)\kappa_j | x\in\Omega\}\right|_{\max} \quad \forall i,j,$$

where $|\cdot|_{\max}$ denotes the maximum of the absolute value. The Fourier transform is used to avoid a discretization term.

The resulting convolutions in the nonlinear relations can be avoided with further transformations and inverse transformations.

The implicit step remains stable, as long as the denominator is positive. In order to avoid instabilities, oscillations smaller than the lattice spacing λ are cut. For this, a $\lambda_{\text{cut}} > \lambda$ is chosen and the values in the Fourier space are set to zero, if $|\boldsymbol{k}| < 2\pi/\lambda_{\text{cut}}$. To depress the occurrence of ringing there are smooth cutting functions available. For our purpose, a linear function is sufficient

$$w(|\boldsymbol{k}|) := \begin{cases}1, & |\boldsymbol{k}| \le k_1,\\ 1-\dfrac{(|\boldsymbol{k}|-k_1)^2}{(k_2-k_1)^2}, & k_1 < |\boldsymbol{k}| < k_2,\\ 0, & k_2 \le |\boldsymbol{k}|.\end{cases}\tag{17}$$

As described above, the condition $\sum_j^K c_j = 1$ has to be fulfilled. Hence the last component can be specified by $c_K = 1 - \sum_i^{K-1} c_i$. However, the error which is caused by the cutting sums up for the computation of c_K. Therefore, all concentration fields have to be calculated. To avoid a continuous increase of the numerical error, it has to be ensured that $\boldsymbol{c}\in\mathcal{C}^\Delta$ by normalizing $\boldsymbol{c}$. Since concentrations close to zero in Eq. (15) cause instabilities, a lower bound, $s := 10^{-4}$, is introduced for the concentrations, i.e. concentrations $< s$ are set to s. Concentrations adapted in this way do not change during the normalization of $\boldsymbol{c}$.

The total memory required for d dimensions and K components, corresponds to $2 + K(2 + 4d)$ real fields and $3 + K(4 + 3d)$ Fourier transforms are required.

3. Analytical solution of the free energy

We aim to formulate the density $\psi(\boldsymbol{r})$ of a perfect crystal, i.e. a crystal with the minimal free energy. We divide the free energy of a MPFC unit cell (35) for constant concentrations $\boldsymbol{c}$ into a potential and a correlation part

$$F = \frac{1}{V}\int_\Omega \underbrace{\frac{n^2}{2} - \eta\frac{n^3}{6} + \chi\frac{n^4}{12} + \omega\Delta F_{\mathrm{mix}}(n+1)}_{=:f_{\mathrm{pot}}} \underbrace{-\frac{1}{2}n\int C_{\mathrm{eff}}(|\boldsymbol{r}-\boldsymbol{r}'|)n'\,\mathrm{d}\boldsymbol{r}'}_{=:f_{\mathrm{corr}}}\,\mathrm{d}\boldsymbol{r}, \tag{18}$$

where $V := \int_\Omega \mathrm{d}\boldsymbol{r}$ represents the volume of the unit cell.

The density can be approximated by

$$\psi(\boldsymbol{r}) = \sum_j A_j \sum_{\boldsymbol{k}_j\in \mathrm{K}_j} \exp(iq\boldsymbol{k}_j\cdot\boldsymbol{r}),$$

where lattice vectors $\boldsymbol{k}_j$ with equal length are combined into shells K_j, to which an amplitude A_j can be assigned. q is the reciprocal lattice constant. For the n^4 part of the potential, this results in

$$n(\boldsymbol{r})^4 = \sum_j A_j \sum_{\boldsymbol{k}_j\in K_j}\exp(iq\boldsymbol{k}_j\cdot\boldsymbol{r})\cdot\sum_k A_k\sum_{\boldsymbol{k}_k\in K_k}\exp(iq\boldsymbol{k}_k\cdot\boldsymbol{r})\cdot\sum_l A_l\sum_{\boldsymbol{k}_l\in K_l}\exp(iq\boldsymbol{k}_l\cdot\boldsymbol{r})\cdot\sum_m A_m\sum_{\boldsymbol{k}_m\in K_m}\exp(iq\boldsymbol{k}_m\cdot\boldsymbol{r})$$
$$= \sum_{j,k,l,m} A_jA_kA_lA_m \sum_{\boldsymbol{k}_j\in K_j,\boldsymbol{k}_k\in K_k,\boldsymbol{k}_l\in K_l,\boldsymbol{k}_m\in K_m}\exp(iq(\boldsymbol{k}_j+\boldsymbol{k}_k+\boldsymbol{k}_l+\boldsymbol{k}_m)\cdot\boldsymbol{r})$$

where either $\boldsymbol{v} := (\boldsymbol{k}_j+\boldsymbol{k}_k+\boldsymbol{k}_l+\boldsymbol{k}_m) = 0$ or there is a $\boldsymbol{v}' := (\boldsymbol{k}'_j+\boldsymbol{k}'_k+\boldsymbol{k}'_l+\boldsymbol{k}'_{m'})$ with $\boldsymbol{k}'_j,\boldsymbol{k}'_k,\boldsymbol{k}'_l,\boldsymbol{k}'_m$ from the same shells, so that $\boldsymbol{v} = -\boldsymbol{v}'$ and with this $\exp(iq\boldsymbol{v}\cdot\boldsymbol{r}) + \exp(iq\boldsymbol{v}'\cdot\boldsymbol{r}) = 0$ for all $\boldsymbol{r}$. We introduce $N_{jklm} \in \mathrm{N}$ the number of contributing combinations. It follows

$$n(\boldsymbol{r})^4 = \sum_{j,k,l,m} A_jA_kA_lA_mN_{jklm}.$$

We further write

$$\frac{1}{V}\int_\Omega a_4 n(\boldsymbol{r})^4\,\mathrm{d}\boldsymbol{r} = a_4\sum_{j,k,l,m}A_jA_kA_lA_mN_{jklm}.$$

A similar expression results for $n^3(\boldsymbol{r})$ as

$$\frac{1}{V}\int_V n^3(\boldsymbol{r})\,\mathrm{d}\boldsymbol{r} = \sum_{j,k,l}A_jA_kA_lN_{jkl},$$

with $N_{jkl} \in \mathrm{N}$. For $n^2(\boldsymbol{r})$, either $\boldsymbol{k}_j+\boldsymbol{k}_l = 0$ applies for $\boldsymbol{k}_j, \boldsymbol{k}_l$ from the same shells, or a negative contribution yields to a canceling of exponential functions. We obtain

$$\frac{1}{V}\int_V n^2(\boldsymbol{r})\,\mathrm{d}\boldsymbol{r} = \sum_j A_j^2N_j,$$

whereby $N_j \in \mathrm{N}$ represents the number of vectors in K_j. We further derive

$$\frac{1}{V}\int_V n(\boldsymbol{r})\,\mathrm{d}\boldsymbol{r} = \sum_j A_j\sum_{\boldsymbol{k}_j\in\mathrm{K}_j}\exp(iq\boldsymbol{k}_j\cdot\boldsymbol{r})\frac{1}{V}\int_V\mathrm{d}\boldsymbol{r} = A_0,$$

since for $j > 0$ there is a $\boldsymbol{k}'\in\mathrm{K}_j$ with $\boldsymbol{k} = -\boldsymbol{k}'$ for each $\boldsymbol{k}\in\mathrm{K}_j$ and so $\exp(iq\boldsymbol{k}\cdot\boldsymbol{r}) + \exp(iq\boldsymbol{k}'\cdot\boldsymbol{r}) = 0$ for all $\boldsymbol{r}$.

The correlation is calculated numerically. For this purpose, a unit cell is approximated by means of a finite number, N, of modes according to

$$n(\boldsymbol{r}) = \sum_{j=0}^{N} A_j\sum_{\boldsymbol{k}_j\in\mathrm{K}_j}\exp(iq\boldsymbol{k}_j\cdot\boldsymbol{r}). \tag{19}$$

With Fourier transforms, the convolution is avoided and integrated numerically

$$F_{\mathrm{corr}} := \frac{1}{V}\int_\Omega n(\boldsymbol{r})\cdot C_{\mathrm{eff}}{*}n(\boldsymbol{r})\,\mathrm{d}\boldsymbol{r} = \frac{1}{V}\int_\Omega n(\boldsymbol{r})\mathcal{F}^{-1}\left(\widehat{C}_{\mathrm{eff}}\cdot\mathcal{F}(n(\boldsymbol{r}))\right)\mathrm{d}\boldsymbol{r}.$$

By inserting the previous equations, the free energy in Eq. (18) depending on q and $\boldsymbol{A}$ can be reformulated in the form

$$F(q,\boldsymbol{A},\boldsymbol{c}) = \frac{1}{2}\sum_j A_j^2N_j - \frac{\eta}{6}\sum_{j,k,l}A_jA_kA_lN_{jkl} + \frac{\chi}{12}\sum_{j,k,l,m}A_jA_kA_lA_mN_{jklm} + \omega\Delta F_{\mathrm{mix}}(A_0+1) - \frac{1}{2}F_{\mathrm{corr}}. \tag{20}$$

3.1. Phase diagram

We denote $\mathcal{C}^\Delta$ to be the simplex of the concentrations. For the construction of a ternary phase diagram, the free energies of the single phases depending on $\boldsymbol{c}\in\mathcal{C}^\Delta$ are required. The liquid phase has a constant density, so that $A_j = 0$ for all $j > 0$ and hence, Eq. (19) simplifies to $n(\boldsymbol{r}) = A_0$. Our mean density in particular is $A_0 = 0$. Inserting this into Eq. (20) results in

$$F_\ell(q,\boldsymbol{A},\boldsymbol{c}) = F_\ell(\boldsymbol{c}) = \omega\Delta F_{\mathrm{mix}}.$$

The single solid phases can not be calculated directly from the density field or the concentration fields. However, the free energy potential $F_s(\boldsymbol{c})$ of the solid phases can be determined on $\mathcal{C}^\Delta$ and hence the phase diagrams can be derived, as described in Sec. 3.2.

The calculation of $F_s(\boldsymbol{c})$ can either be done numerically or approximately. In the numerical version, a crystal is simulated and its free energy is integrated numerically. Alternatively, the approximate free energy of Eq. (20) is minimized in q and the vector $\boldsymbol{A}$ for N shells. At first, we deal with the numerical solution.

3.1.1. Minimization

For the calculation of the free energy, the simulation of one single unit cell is sufficient. As initial density, Eq. (19) is placed in a simulation domain with 16×16 grid cells, with the mean density $A_0 = 0$ for $N = 1$. In order to initialize the crystal without tensile stress and pressure load, the lattice spacing $\Delta x = a/16$ is chosen with $a = 2\pi/q$. The free energy of a density distribution can be determined by means of a numerical integration of Eq. (18). The simulations of the evolution equation Eq. (16) are carried out until the *converged density* is reached. We define the density as convergent, if the change of the free energy between two time steps Δf is smaller than 10^{-7}, which is defined as the convergence barrier. We designate the free energy, calculated from the converged density of a simulation with the lattice constant q, as $f(q)$. The minimal free energy $f_{\min}$ is reached for $q_{\min}$. We remark that $f(q)$ is not dependent on the selection of A_1, as long as the density does not converge towards a constant density, which happens if A_1 is either too large or too small. We use $A_1 = 0.23$.

Under free boundary conditions, a non-perfect crystal changes its lattice constant to $q_{\min}$, to approach a perfect crystal. However, the lattice constant is fixed during the simulation, so that the crystal is exposed to tensile stresses and pressure loads.

The minimization of $f(q)$ is equivalent to $f'(q) = 0$. For this purpose, we employ central finite differences

$$f'(q) := \frac{f(q+\Delta q) - f(q-\Delta q)}{2\Delta q},$$

with $\Delta q = 0.0001$. In order to solve $f'(q) = 0$, we use the Brent algorithm [24,25], which is a root finding algorithm working without derivatives. To initialize the Brent algorithm we use the q found by a scan for the smallest free energy. Therefor we perform simulations in a range of around $q = 5.5$ to 7 by steps of 0.05. A manual visual view of the simulation checks that the q of the minimal free energy results in one unit cell, if not there is another local minimum for this. The Brent algorithm will not leave the local minimum. In each iteration step, two simulations $f(q + \Delta q)$ and $f(q - \Delta q)$ are carried out. If $|f'(q)| < 10^{-6}$, we accept q as minimum. The Brent algorithm usually terminates after less than $10 - 15$ iterations. However, since we need converged simulations, the calculation of a free energy takes several minutes. With this algorithm, a closely meshed scan of $\mathcal{C}^{\Delta}$ is very time-consuming and motivates the necessity of a more efficient algorithm discussed next.

3.1.2. Simulated annealing algorithm

To avoid computationally intense simulations, we use the approximated free energy in Eq. (20). For N shells, this is a $N + 1$-dimensional optimization problem, so that we use the heuristic optimization algorithm *simulated annealing*. The advantage of this algorithm is, that a local minimum can remain with a certain probability in order to find a better approximation towards the minimum. However, an acceptable minimum is not reached with every attempt. It happens, that $F_{\text{approx}} \approx F_{\ell}$. Since the algorithm does find different local minima during different attempts, the found minimum with 20 attempts is often acceptably low.

Fig. 2 shows this method for different N-mode approximations, with 20 attempts each. With increasing N, the approximated free energy decreases. With $N = 10$ to 14 an accumulation occurs. A comparison with the Brent method from Sec. 3.1.1 shows, that this minimization is already reached approximately with $6 - 7$ shells. It is also shown, however, that a 2-mode approximation is not good enough.

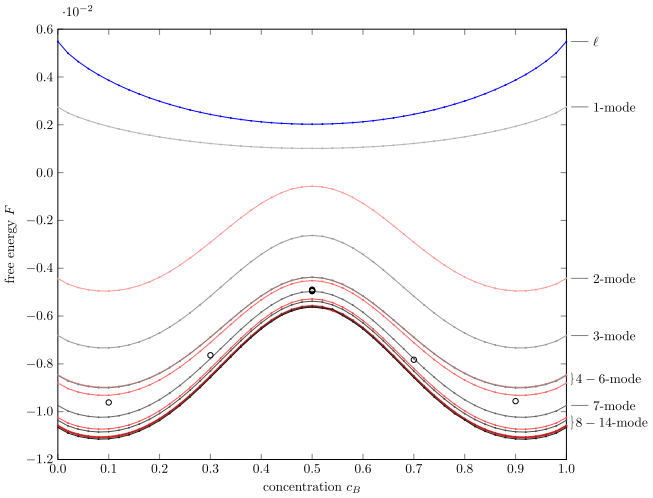

Fig. 2. Free energies for $c_A = 0$ proposed by the approximation method for $1 - 14$ shells and 20 attempts (lines) in comparison with minimization results from Sec. 3.1.1 for $c_A = 0.01$ (circles).

Fig. 3 compares the errors of the different minimization methods. We observe that the free energy is subject to fluctuations that are significantly lower than the fluctuations of the reciprocal lattice constant. For the Brent method, the inner error bars show the error, which is caused by the choice of $\Delta q = 0.0001$. The simulations are stopped by the predefined convergence barriers 10^{-7} and 10^{-9}. Simulation domains with an edge length of 16 and 32 are used (see Table 1). The free energy determined with the Brent method is subject to some inaccuracies. Hence, we can well assume, that the real free energy is even a bit lower. The runtime of the Brent method (Table 1) is about six times longer than with the approximation (Table 2). The calculation for more shells lasts longer, so we use 12 shells.

For $\boldsymbol{A} = 0$, F_s becomes F_{ℓ}, whereby the free energy of the crystal can only be determined at the positions where $F_s < F_{\ell}$. A lower bound s with $s < |A_1|$ is introduced, in order to enlarge the area a bit. Higher amplitudes are restricted with $s < 2^j |A_j|$. Therefore, the domain in the algorithm is adapted as $D = [-s, s] \times [-s/2, s/2] \times \cdots$. This is not possible with the Brent method from Sec. 3.1.1. The choice of $s = 0.075$ ensures, that F_s is not influenced in the area of $F_s < F_{\ell}$, but nevertheless it ensures, that the profile of the free energy can be extended to this area.

3.1.3. Analytical solution

According to Eq. (20), we see that a minimization with respect to q involves the minimization of F_{corr}. In particular, $\widehat{C}_{\text{eff}}$ is only dependent on q. There, $\widehat{C}_{\text{eff}}$ is an interpolation of the individual correlation functions

$$\widehat{C}_{\text{eff}} = \sum_{i=1}^{3} h_i(\boldsymbol{c}) \widehat{C}_2^{ii}$$

in which each correlation function is the maximum of two peaks, as defined in Eq. (14). In a pure material, k_{i1} is defined as reciprocal lattice constant, so that $q_{\min}$ is determined by the first peak. The interpolation results in new peaks, whereby the position depends on the proportion of the single components. If the first peaks of all correlation functions are positioned on the left side of the point of discontinuity, which is caused by the maximum, the position of the first interpolated peak is not influenced. This is given for our

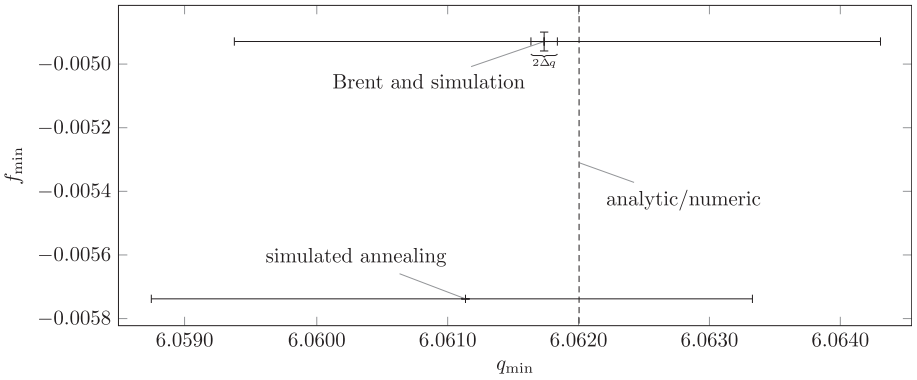

Fig. 3. Error tolerances for $\boldsymbol{c} = (0.01, 0.5, 0.49)$ of the minimal free energy $f_{\min}$ and the reciprocal lattice constant $q_{\min}$ determined with simulated annealing (5×20 attempts), Brent/simulations (16^2 and 32^2 cells, as well as convergence barrier 10^{-7} and 10^{-9}) and numerical solution of the first peak of the correlation function C_{eff}.

example, as shown in Fig. 1. In order to find $q_{\min}$, it is sufficient to calculate the maximum of the interpolation of the first peaks. Since $\widehat{C}_{\text{eff}}$ from the first peaks is a function which is continuously differentiable, $\frac{\partial \widehat{C}_{\text{eff}}(k)}{\partial k} = 0$ can be solved. The solution for $\boldsymbol{c} = (0.01, 0.5, 0.49)$ is plotted as a vertical line in Fig. 3 and lies in the range of the solutions of the other two methods. $q_{\min}$, which is solved in this way, can be used as initial value for the search for the amplitudes A_i.

Fig. 4 displays the process of approximating $q_{\min}$ as the first peaks k_{i1} for different concentrations $\boldsymbol{c}$, related to the corners of the ternary phase diagram.

3.2. Common tangent plane construction

For the solid phases, we determine the free energy by means of the above methods for a particular temperature σ. For this purpose, we scan the domain of the simplex $\mathcal{C}^{\Delta}$ with a step width of 0.02 in c_A- and c_B-direction. At the corners of the simplex $\mathcal{C}^{\Delta}$, there is $F_s < F_\ell$ which means, that the single solid phases are the stable phases in these areas. We approximate the free energy to profiles of the solid phases i, with the paraboloids $W_i(x, y) := a_i(x - u_i)^2 + b_i(y - v_i)^2 + c_i$. Fig. 5 shows the potential F_ℓ, as well as the calculated points of the F_s potentials in red.

In the area of the points marked in blue, F_s is fitted by W_i. In the following, the paraboloids W_i are used as free energy of the solid phase i. They are chosen in such a way, that they are in good agreement in the regions around the common tangent planes. For the determination of the equilibria between the solid and liquid phase, we calculate the common tangent planes between F_ℓ and W_i.

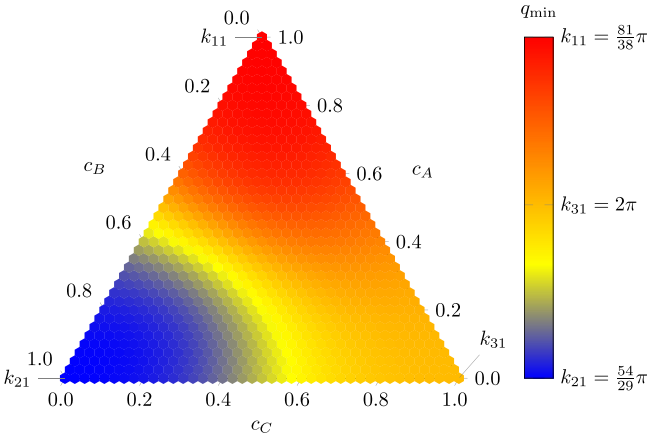

Fig. 4. Representation of $q_{\min}$ as color value over the concentration distribution $\boldsymbol{c}$, from k_{21} over k_{31} to k_{11}.

Table 1
Minimal reciprocal lattice constant q and averaged free energy $\bar{f}(q) := \frac{f(q-\Delta q)+f(q+\Delta q)}{2}$, as well as iteration steps and runtime t of the Brent method for different convergence barriers Γ and number of cells N_x and $\boldsymbol{c} = (0.01, 0.5, 0.49)$.

Γ	N_x	q	$\bar{f}(q)$	iter.	t [s]
10^{-7}	16	6.061	$-4.910 \cdot 10^{-3}$	13	226
10^{-9}	16	6.062	$-4.959 \cdot 10^{-3}$	15	470
10^{-7}	32	6.059	$-4.899 \cdot 10^{-3}$	9	220
10^{-9}	32	6.064	$-4.948 \cdot 10^{-3}$	13	527

Table 2
Minimal reciprocal lattice constant q and free energy $F(q)$, as well as best (second best) attempt and runtime t of the simulated annealing algorithm for $\boldsymbol{c} = (0.01, 0.5, 0.49)$ and $N = 12$ with 20 attempts, respectively.

q	$F(q)$	attempt	t [s]
6.060	$-5.738 \cdot 10^{-3}$	16(9)	37.4
6.061	$-5.738 \cdot 10^{-3}$	18(1)	39.3
6.064	$-5.738 \cdot 10^{-3}$	8(4)	31.3
6.062	$-5.738 \cdot 10^{-3}$	6(3)	33.7
6.059	$-5.738 \cdot 10^{-3}$	12(10)	37.3

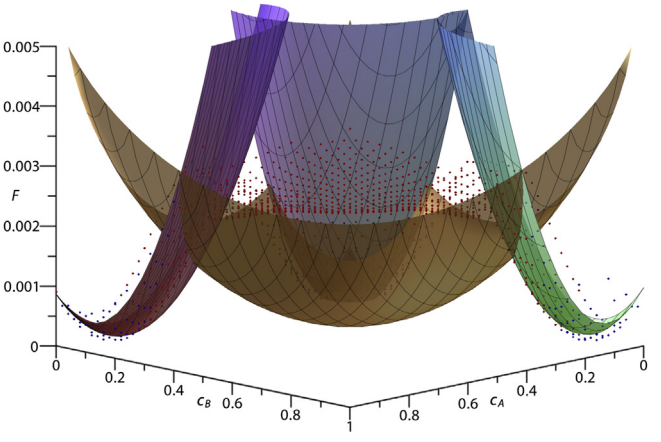

Fig. 5. Plot of the free energy potential of the liquid phase F_ℓ (gold) and of the approximated potential F_s of the solid phases (red points) with paraboloids W_i of the solid phases F_i. The potentials are fitted over the points marked in blue in the simplex corners. The diagram illustrates the Cartesian projection of $\mathcal{C}^{\Delta}$.

For this purpose, we first calculate the chemical potentials in c_A- and c_B-direction by

$$\mu_\alpha^s := \frac{\partial F_s(c_A, c_B)}{\partial c_A}, \mu_\beta^s := \frac{\partial F_s(c_A, c_B)}{\partial c_B},$$

$$\mu_\alpha^\ell := \frac{\partial F_\ell(c_A, c_B)}{\partial c_A}, \mu_\beta^\ell := \frac{\partial F_\ell(c_A, c_B)}{\partial c_B},$$

where, $\cdot_\alpha$ denotes the c_A-direction, $\cdot_\beta$ designates the c_B-direction, $\bullet^s$ represents the solid phase and $\cdot^\ell$ is the liquid phase.

The equilibrium planes have the same slopes in the point of equilibrium of the solid phase $\boldsymbol{c}^s = (c_A^s, c_B^s, c_C^s)$ and the liquid phase $\boldsymbol{c}^\ell = (c_A^\ell, c_B^\ell, c_C^\ell)$, such that we get

$$\mu_\alpha^s(c_A^s, c_B^s) = \mu_\alpha^\ell(c_A^\ell, c_B^\ell), \quad \mu_\beta^s(c_A^s, c_B^s) = \mu_\beta^\ell(c_A^\ell, c_B^\ell).$$

The grand potentials, too, must be equal, reading

$$\begin{aligned} &F_s(c_A^s, c_B^s) - \mu_\alpha^s(c_A^s, c_B^s)c_A^s - \mu_\beta^s(c_A^s, c_B^s)c_B^s \\ &\quad = F_\ell(c_A^\ell, c_B^\ell) - \mu_\alpha^s(c_A^\ell, c_B^\ell)c_A^\ell - \mu_\beta^s(c_A^\ell, c_B^\ell)c_B^\ell. \end{aligned}$$

We obtain the solution of these equations for the concentrations c_A^s, c_A^ℓ, c_B^s and c_B^ℓ, by retaining either the parameter c_A^ℓ or c_B^ℓ and by calculating the remaining parameters. To get the equilibrium lines, the retained parameter is varied in 0.01 steps.

Fig. 6 displays the calculated phase diagrams for σ between 0.215 and 0.23. The intersection points of the three liquidus curves meet at one point $\sigma = 0.2235$, representing the eutectic temperature according to these calculations. As a comparison, we show the calculated phase diagrams for this eutectic temperature and 4 shells in Fig. 6, which emphasizes that the approximation is strongly dependent on the number of approximated shells.

4. Applications

For the application of the multi-component PFC model, we use the system Al–Cu–Mg, as proposed by Ofori–Opoku et al. [1]. The three correlation functions (Cu, Mg, Al) are each composed of two peaks in the form of Eq. (13), with $k_{11} = 81\pi/38$, $k_{21} = 54\pi/29$, $k_{31} = 2\pi$ and $k_{i2} = \sqrt{2}k_{i1}$, as well as $\sigma_{Mij} = 0.55$, $\alpha_{i1} = 0.8$ and $\alpha_{i2} = \sqrt{2}\alpha_{i1}$ $\forall i,j$. The free simulation parameters are $\chi = 1$, $\eta = 1.4$ and $\omega = 0.005$. The reference densities are chosen as $c_1^0 = c_2^0 = 0.333$ and the mobilities are all equal with $M_n = M_j = 1$.

4.1. Influence of the interpolated correlation function

For the three interpolation functions of the effective correlation function, we perform simulations of planar growth of an Al-rich phase in an undercooled melt. 16 unit cells of a crystal phase are

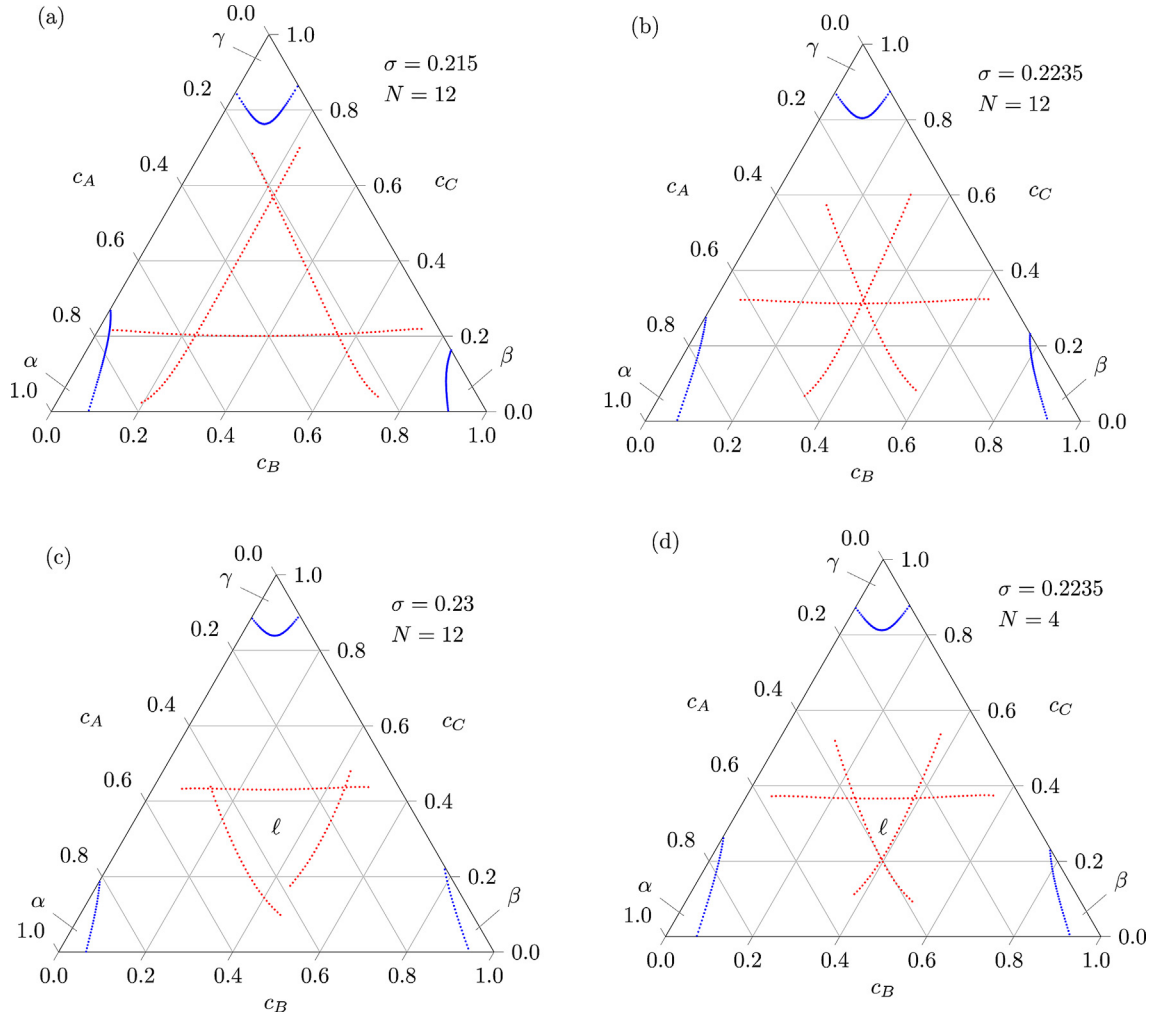

Fig. 6. Ternary phase diagrams with 12 shells calculated for (a)–(c) $\sigma = 0.215$, 0.2235 and 0.23. With the eutectic temperature at around $\sigma_E = 0.2235$. (d) 4 shells at σ_E.

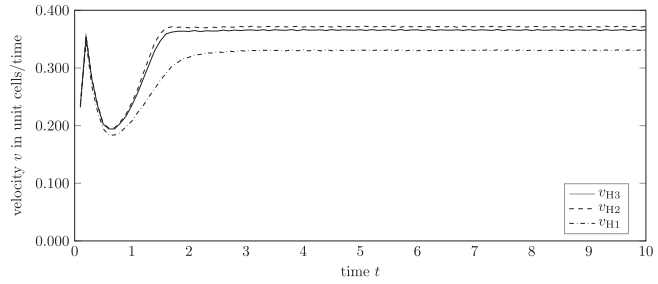

Fig. 7. Velocity of the interface of a 2D planar front for various interpolation functions.

set in a melt inside a domain with 4096 × 16 cells or 256 × 1 unit cells. The initial concentration is chosen as $\boldsymbol{c} = (c_{\mathrm{Cu}}, c_{\mathrm{Mg}}, c_{\mathrm{Al}}) = (0.1, 0.1, 0.8)$. The lattice width is calculated by an energy minimization for the given parameter such that the crystal is set without stress influences from the boundary. We get the reciprocal lattice constants $q_{\mathrm{H1}} = 6.282807$, $q_{\mathrm{H2}} = 6.280986$ and $q_{\mathrm{H3}} = 6.280985$. The time step width is $\Delta t = 0.001$ to hold stable simulations for each interpolation function. The effective temperature reads $\sigma = 0.17$ and the gradient terms are chosen as $\kappa_j = 1$.

The simulations run until the growth rate reaches a steady-state growth. The interface between crystal and melt is detected and the velocity of its movement is shown in Fig. 7.

After the relaxation of the one mode filling (at $t \approx 1$) the interface velocity increases until it reaches the steady-state growth (at $t \approx 2$). The steady-state velocities for the interpolation function (H2) and (H3) are very similar and, in dimensional units, read $v_{(\mathrm{H2})} = 0.37$ and $v_{(\mathrm{H3})} = 0.36$ unit cells per time. Only (H1) shows a deviation from these velocities with $v_{(\mathrm{H1})} = 0.33$. These results show the influence of the growth kinetics by the interpolation function. As shown in Fig. 1, the correlation function depends on the interpolation function and the velocity of the growth depends on the correlation function. The effective temperature σ changes the width of the peaks. On the other hand, if the interpolation of the correlation function changes the width of the peaks, the effective temperature is changed and hence the undercooling is changed as well. Thus, it is expected that it also changes the growth rate.

In the further applications, we use the interpolation function (H2).

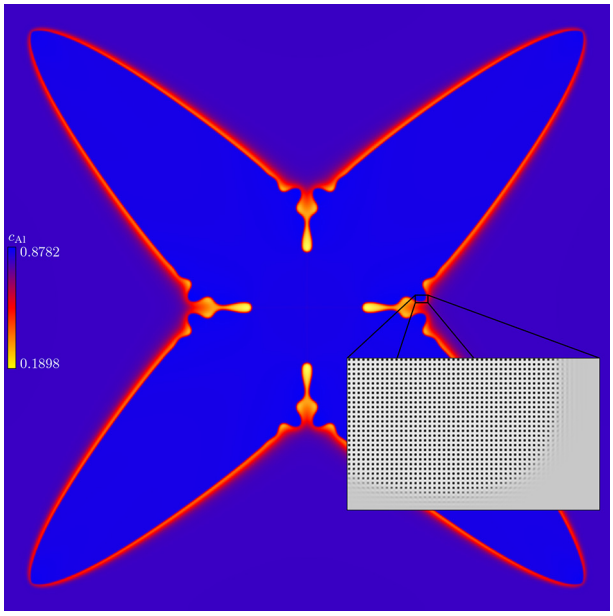

Fig. 8. Al concentration field after 37,000 time steps. The enlarged part shows the density field.

4.2. Dendritic growth in 2D

An Al-rich nucleus is simulated in an undercooled melt. The nucleus with the size of 10 × 10 atoms, is placed as a square sq crystal in the center of a domain with 20,480 × 20,480 cells. The initial concentration of the melt and the nucleus is $\boldsymbol{c} = (c_{\mathrm{Cu}}, c_{\mathrm{Mg}}, c_{\mathrm{Al}}) = (0.1, 0.1, 0.8)$. The lattice width is $\Delta x = 0.125$ and the time step width is $\Delta t = 3$. The effective temperature reads $\sigma = 0.182$ and the gradient terms are chosen as $\kappa_j = 1$. Fig. 8 shows the grown dendrite after 37,000 time steps after a computing time of 23 days on a computer node with two AMD Opteron 6344 with 12 cores each, at 2.9 GHz and 32 GB of random access memory.

4.3. Dendritic growth in 3D

The application in 3D requires different correlation functions since the sq lattice turns into the fcc lattice formed from aluminum. We continue to consider a model type system, although we adapt the correlation functions to the atomic properties of the elements. The mass is defined as $m = n \cdot A$ with the number of atoms per unit cell n and the relative atomic mass A. The volume of a unit cell is given by $V = a^3$, where a is the lattice constant. The density is $\rho = m/V = nA/a^3$. The atomic unit of mass is $1\,u = 1.660538921 \cdot 10^{-27}\,kg$. Table 3 composes the relative atomic mass, the density, the lattice constant a and the plane distance $\tilde{\lambda}$, which is normalized to Al.

The plane distances are scaled with $\tilde{\lambda}$ and yield $\lambda_1 = a/\sqrt{3}$ and $\lambda_2 = 1/2$. With $k = 2\pi/\lambda$, the peaks of the correlation functions (Mg, Cu, Al) result in $k_{11} = 0.893\sqrt{3}2\pi$, $k_{21} = 1.119\sqrt{3}2\pi$, $k_{31} = \sqrt{3}2\pi$ and k_{i2} accordingly. The quantities σ_{Mij}, α_{ij} and κ_j remain as for 2D. We apply the cutting function in Eq. (17) with $k_1 = 1$ and $k_2 = 1.25$. The simulation domain contains 640 × 640 × 640 cells with $\Delta x = 0.0894521496$ and $\Delta t = 0.002$. The initial concentration is $\boldsymbol{c} = (0.7, 0.15, 0.15)$. A spherical atomic cluster with an fcc lattice structure and an inner radius of 35 cells is constructed. The density field decreases linearly until a radius of up to 47 cells is reached. The effective temperature is $\sigma = 0.18$. Fig. 9 visualizes the dendrite after 2300 time steps after a computing time of 3 days on a computer with 2 Intel Xeon E5649 processors with 6 cores each, at 2.53 GHz and 96 GB of random access memory.

For the dendritic structure to be recognized, the simulation area has to be much larger. As described above, the simulations require the memory of 44 real fields which is 86 GB for an edge length of 640 cells. Doubling the memory leads to an edge length of 806 cells. The methods of FFTW used for the parallelization are performant in the shared memory parallelization, which prevents a simple switch to cluster systems.

4.4. Lamellar eutectic growth

At conditions close to the eutectic temperature $\sigma_{\mathrm{e}} = 0.2235$ (see Fig. 6), the growth of ternary eutectic lamellae with three distinct

Table 3
Atomic properties of the ternary system.

Atom	$A[u]$	$\rho[\mathrm{u/m^3}]$	$a[nm]$	$\tilde{\lambda}$
Al	26.982	2.7	40.49	1
Cu	63.546	8.92	36.17	0.893
Mg	24.305	1.738	45.29	1.119

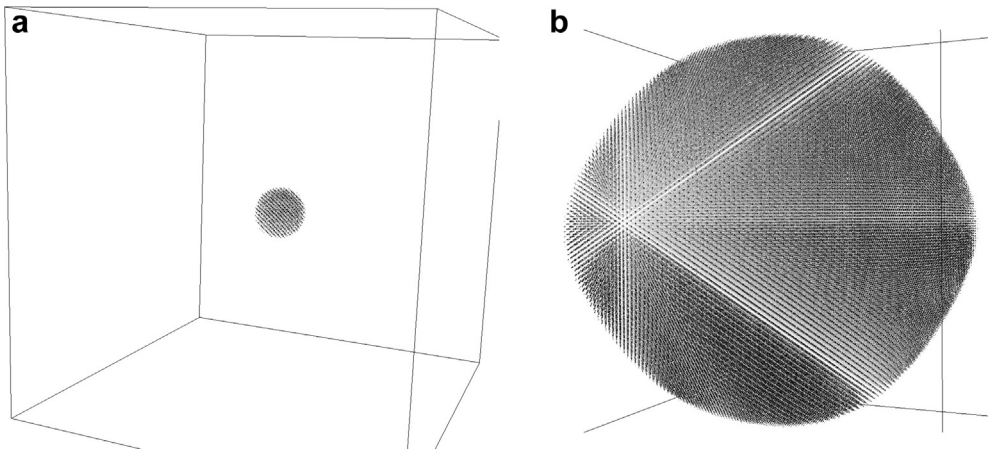

Fig. 9. Isosurfaces of the density field (a) at the beginning and (b) after $t = 2300$ time steps of the PFC simulation. The simulation box with $640 \times 640 \times 640$ cells covers 140,000 atoms.

solid phases (α, β, γ) evolving from undercooled meld is retrieved with the multi-component PFC simulations. The 2D model system is used to arrange lamellae with the crystal structure of one component each with high concentration next to each other. The melt is consists of the same proportions of the three components Al, Ag and Mg. The simulation is performed at the effective temperature $\sigma = 0.2$, which is below the ternary eutectic temperature. The three kinds of atoms have different interatomic distances. Since the simulation domain is periodically continued, the lamellae are placed in a stress-free environment by setting an equal number of 30 atoms for each component and by adapting the lattice width accordingly. This results in $\Delta x = 0.091874015$ for a domain of 1365×1024 cells. Between the single lamellae, an interface is formed, similar as in the solid–liquid system, with the difference, that the width is not known from the simulations, due to the different lattice constants. Hence, the solid phases cannot be initialized completely stress-free. In order to prevent the stress from being too large, several atoms are set next to each other, so that the error spreads across all atoms. The maximum is, that one defect can be made by half of an atom. With 30 atoms, this corresponds to an average maximum error of <1.7%. In addition, the lamellae are arranged in the sequence β–α–γ–α where α, β, γ correspond to the Al-, Cu-, Mg rich solid phases. A symmetrical structure is formed due to the periodicity of the phase ordering. The

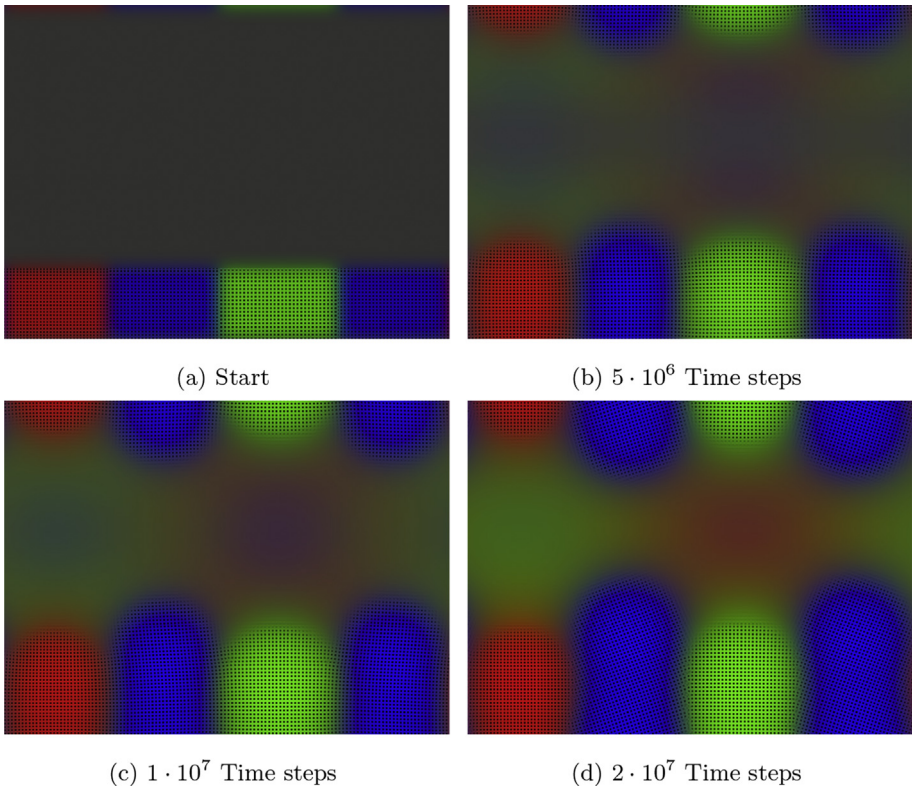

Fig. 10. Lamellar growth for $\sigma = 0.2$ below the eutectic temperature. The peaks of the density field are marked in black. The concentration coloring refers to Cu (red), Mg (green) and Al (blue) and mixtures correspond to the RGB values.

single lamellae have a height of around 18 atomic layers, as shown in Fig. 10(a). The concentration field evolves much slower than the density field. It restricts the time step severely, because of the larger nonlinear part, so that the time step width is $\Delta t = 0.0004$. The frequencies are roughly cut at 1.0 and we chose $\kappa_j = 5$.

The formation of the three eutectic solid phases is recorded in Fig. 10. For the $2 \cdot 10^7$ time steps in total, the simulation ran for around 16 weeks on a computer node with two AMD Opteron 6344 with 12 cores each, at 2.9 GHz and 24 GB of random access memory. Each concentration field is assigned to a basic color and is considered as a single RGB color channel. According to this, the liquid phase, which is an equally proportional mixture of the 3 concentrations, is gray. The respective complementary colors can be recognized in front of the lamellae resulting from the lack of the respective concentration. In the subsequent course of the simulations, the concentration field extends, so that the periodic boundary conditions influence the lamellar growth mode. The Al lamellae (blue) are the fastest growing leading to an additional depletion of the concentration in front of the other lamellae. This is reflected in the enrichment of Mg (green) in the liquid phase, in front of the Cu lamella (red) and vice versa. Since the crystal lattices of the different lamellae do not match, lattice defects occur at the interface between the lamellae. These defects rearrange during the simulation. Fig. 10(d) shows the Al lamellae with a rotated orientation. The lattice structure of the density field is recovered in regions where a single component has a high concentration. The density field evolves much faster than the concentration field. For fixed concentrations, the crystal evolves within 5000 time steps ($\Delta t = 0.002$) across the whole area.

5. Conclusion

In this work we discuss, that the free energy calculation depends on the number of shells. The common usage of two shells is not sufficient. Six to seven shells archive good results in comparison with the free energy from a simulated crystal. At approximately 12 shells, the free energy is bounded. For a ternary phase diagram we exemplarily demonstrate high derivations for different number of shells. For 12 shells an eutectic point is established, whereas the phase diagram for the same temperature with only 4 shells has a large area of liquid phase.

The simplification of the correlation functions into one effective expression C_{eff}, defined as an interpolation of the pairwise correlation functions of the single components leads to the fact, that only these have to be known. The numerics of the semi-implicit spectral method shows that the last concentration field cannot be omitted. From the Onsager reciprocal relations it follows that a system of equations depending only on the number of components has to be solved for each implicit step. Since C_{eff} is dependent on the interpolation, it is essential to employ an efficient interpolation function for the effective correlation function. During a permutation of the components, for instance, Eq. (H1) provides different results. The interpolation presented in Eq. (H2) avoids this deficiency. However, we show that the velocity of growth depends on the chosen interpolation function. This must be taken into account in further studies.

As shown in the simulations, the concentration fields evolve much slower than the density field. In the semi-implicit spectral solution, the non linearity of the concentration equations requires $3 + K(4 + 3d)$ Fourier transforms and the memory of $2 + K(2 + 4d)$ fields for d dimensions and K concentrations. Dendritic growth for Al-rich melts is reported in 2D and 3D. Due to the huge computational effort associated with the 3D simulations, the formation of side arms is not resolved in the considered time interval. Lamellar growth of three solid phases in a ternary system close to the eutectic temperature is simulated in 2D. The equally distributed concentrations of the melt clearly demonstrate the slow evolution of the concentration fields.

Acknowledgments

The authors gratefully acknowledge the financial support by the German Research Foundation (DFG) in the Priority Program SPP 1296.

Appendix A. Weighted interpolation

In this appendix we describe the weighted interpolation used for the effective correlation function. We list the properties and prerequisites for different interpolation functions.

We consider $\boldsymbol{L} \in \mathrm{R}^n$ to be any value which is weighted by $\boldsymbol{c}$

$$L_{\text{eff}} = \sum_{i=1}^{n} c_i L_i,$$

and assume (h_i) to be a partition of unity, $\sum_{i=1}^{n} h_i(\boldsymbol{c}) = 1$ with a monotonic increase of h_i, $h_i(\boldsymbol{c})\big|_{c_i=0} = 0$ and $h_i(\boldsymbol{c})\big|_{c_i=1} = 1$. Then we can define

$$\tilde{L}_{\text{eff}} = \sum_{i=1}^{n} h_i(\boldsymbol{c}) L_i$$

to be also a weight function of $\boldsymbol{L}$. Normally, $L_{\text{eff}} \neq \tilde{L}_{\text{eff}}$.

Possible weights to fulfill the above equation, are the identity

$$h_i(\boldsymbol{c}) = c_i, \tag{H0}$$

the polynomial expression (cf. [26])

$$h_i(\boldsymbol{c}) = 3c_i^2 - 2c_i^3 + 2c_i \sum_{\substack{j<k \\ j\neq i \\ k\neq i}} c_j c_k, \tag{H1}$$

or the function (cf. [19])

$$h_i(\boldsymbol{c}) = \frac{c_i^2}{\sum_{j=1}^{n} c_j^2}, \tag{H2}$$

which are partially derived. A weighted value

$$\frac{\partial \tilde{L}_{\text{eff}}}{\partial c_j} = \sum_{i=1}^{n} \frac{\partial h_i(\boldsymbol{c})}{\partial c_j} L_i$$

is supposed to be continuous, so that $\frac{\partial h_i(\boldsymbol{c})}{\partial c_j}\big|_{c_i=0} = \frac{\partial h_i(\boldsymbol{c})}{\partial c_j}\big|_{c_i=1} = 0$ and the sum of the changes is supposed to disappear.

The trivial weight in Eq. (H0) does not fulfill these conditions.

The partial derivatives of Eq. (H1) are continuous, in consideration of $c_n = 1 - \sum_{i=1}^{n-1} c_i$. However, the weight is dependent on the selection of the conditional variable. Without the conditional variable, $\frac{\partial h_i(\boldsymbol{c})}{\partial c_j} = 0$ is no longer fulfilled.

The partial derivatives of Eq. (H2) fulfill both, $\sum_i \frac{\partial h_i(\boldsymbol{c})}{\partial c_j} = 0$ as well as $\frac{\partial h_i(\boldsymbol{c})}{\partial c_j}\big|_{c_i=0} = \frac{\partial h_i(\boldsymbol{c})}{\partial c_j}\big|_{c_i=1} = 0$.

References

[1] N. Ofori-Opoku, V. Fallah, M. Greenwood, S. Esmaeili, N. Provatas, Multicomponent phase-field crystal model for structural transformations in metal alloys, Phys. Rev. B 87 (13) (2013) 134105, http://dx.doi.org/10.1103/PhysRevB.87.134105.

[2] M. Berghoff, M. Selzer, B. Nestler, Phase-field simulations at the atomic scale in comparison to molecular dynamics, Sci. World J. 2013 (2013), http://dx.doi.org/10.1155/2013/564272. Article ID 564272.

[3] K.R. Elder, M. Katakowski, M. Haataja, M. Grant, Modeling elasticity in crystal growth, Phys. Rev. Lett. 88 (24) (2002) 245701, http://dx.doi.org/10.1103/PhysRevLett.88.245701.

[4] K.R. Elder, M. Grant, Modeling elastic and plastic deformations in nonequilibrium processing using phase field crystals, Phys. Rev. E 70 (5) (2004) 51605, http://dx.doi.org/10.1103/PhysRevE.70.051605.

[5] J. Swift, P.C. Hohenberg, Hydrodynamic fluctuations at the convective instability, Phys. Rev. A 15 (1) (1977) 319, http://dx.doi.org/10.1103/PhysRevA.15.319.

[6] A. Jaatinen, C.V. Achim, K.R. Elder, T. Ala-Nissila, Phase field crystal study of symmetric tilt grain boundaries of iron, Tech. Mech. 30 (1–3) (2010) 169–176.

[7] A. Jaatinen, C.V. Achim, K.R. Elder, T. Ala-Nissila, Thermodynamics of bcc metals in phase-field-crystal models, Phys. Rev. E 80 (2009) 031602, http://dx.doi.org/10.1103/PhysRevE.80.031602.

[8] K.-A. Wu, A.J. Adland, A. Karma, Phase-field-crystal model for fcc ordering, Phys. Rev. E 81 (6) (2010) 061601, http://dx.doi.org/10.1103/PhysRevE.81.061601.

[9] P.F. Tupper, M. Grant, Phase field crystals as a coarse-graining in time of molecular dynamics, EPL Europhys. Lett. 81 (2008) 40007, http://dx.doi.org/10.1209/0295-5075/81/40007.

[10] S. van Teeffelen, R. Backofen, A. Voigt, H. Löwen, Derivation of the phase-field-crystal model for colloidal solidification, Phys. Rev. E 79 (5) (2009) 051404, http://dx.doi.org/10.1103/PhysRevE.79.051404.

[11] Z.-F. Huang, K.R. Elder, N. Provatas, Phase-field-crystal dynamics for binary systems: derivation from dynamical density functional theory, amplitude equation formalism, and applications to alloy heterostructures, Phys. Rev. E 82 (2) (2010) 021605, http://dx.doi.org/10.1103/PhysRevE.82.021605.

[12] M. Greenwood, N. Ofori-Opoku, J. Rottler, N. Provatas, Modeling structural transformations in binary alloys with phase field crystals, Phys. Rev. B 84 (6) (2011) 064104, http://dx.doi.org/10.1103/PhysRevB.84.064104.

[13] K.R. Elder, N. Provatas, J. Berry, P. Stefanovic, M. Grant, Phase-field crystal modeling and classical density functional theory of freezing, Phys. Rev. B 75 (6) (2007) 064107, http://dx.doi.org/10.1103/PhysRevB.75.064107.

[14] S. Majaniemi, N. Provatas, Deriving surface-energy anisotropy for phenomenological phase-field models of solidification, Phys. Rev. E 79 (1) (2009) 011607, http://dx.doi.org/10.1103/PhysRevE.79.011607.

[15] N. Provatas, S. Majaniemi, Phase-field-crystal calculation of crystal-melt surface tension in binary alloys, Phys. Rev. E 82 (4) (2010) 041601, http://dx.doi.org/10.1103/PhysRevE.82.041601.

[16] K.R. Elder, Z.-F. Huang, N. Provatas, Amplitude expansion of the binary phase-field-crystal model, Phys. Rev. E 81 (1) (2010) 011602, http://dx.doi.org/10.1103/PhysRevE.81.011602.

[17] M. Greenwood, J. Rottler, N. Provatas, Phase-field-crystal methodology for modeling of structural transformations, Phys. Rev. E 83 (3) (2011) 031601, http://dx.doi.org/10.1103/PhysRevE.83.031601.

[18] M. Greenwood, N. Provatas, J. Rottler, Free energy functionals for efficient phase field crystal modeling of structural phase transformations, Phys. Rev. Lett. 105 (4) (2010) 045702, http://dx.doi.org/10.1103/PhysRevLett.105.045702.

[19] N. Moelans, A quantitative and thermodynamically consistent phase-field interpolation function for multi-phase systems, Acta Mater. 59 (3) (2011) 1077–1086, http://dx.doi.org/10.1016/j.actamat.2010.10.038.

[20] R. Folch, M. Plapp, Quantitative phase-field modeling of two-phase growth, Phys. Rev. E 72 (1) (2005) 011602, http://dx.doi.org/10.1103/PhysRevE.72.011602.

[21] L. Onsager, Reciprocal relations in irreversible processes, I., Phys. Rev. 37 (4) (1931) 405, http://dx.doi.org/10.1103/PhysRev.37.405.

[22] B. Nestler, H. Garcke, B. Stinner, Multicomponent alloy solidification: phase-field modeling and simulations, Phys. Rev. E 71 (4) (2005) 041609, http://dx.doi.org/10.1103/PhysRevE.71.041609.

[23] G. Tegze, G.S. Bansel, G.I. Tóth, T. Pusztai, Z. Fan, L. Gránásy, Advanced operator splitting-based semi-implicit spectral method to solve the binary phase-field crystal equations with variable coefficients, J. Comput. Phys. 228 (5) (2009) 1612–1623, http://dx.doi.org/10.1016/j.jcp.2008.11.011.

[24] R.P. Brent, Algorithms for minimization without derivatives, Math. Comput. 28 (127) (1974) 865, http://dx.doi.org/10.2307/2005713.

[25] W.H. Press, S.A. Teukolsky, W.T. Vetterling, B.P. Flannery, Numerical Recipes 3rd Edition: The Art of Scientific Computing, Cambridge University Press, 2007.

[26] A. Choudhury, Quantitative Phase-field Model for Phase Transformations in Multi-component Alloys, Ph.D. thesis, Karlsruher Institut für Technologie, 2012, http://dx.doi.org/10.5445/KSP/1000034598.